RSC Advances

PAPER

View Article Online
View Journal | View Issue

Cite this: *RSC Adv.*, 2025, **15**, 6902

A hybrid scaffold of modified human amniotic membrane with gelatine/dendrimer-protected silver nanoparticles for skin wound healing applications

Mahdi Khalili, [a] Aryan Ekhlasi, [a] Atefeh Solouk, *[a] Masoumeh Haghbin Nazarpak *[b] and Somaye Akbari [c]

The human amniotic membrane (hAM) is a biological material widely utilized to mimic the extracellular matrix in damaged skin. Despite its potential, clinical applications of hAM have been hindered by its poor mechanical properties. Furthermore, cryopreservation process used to store hAM could compromise its inherent bactericidal properties. This study explores an innovative approach by combining hAM with 2, 4, 6 and 8% w/v of gelatine (Gel) and incorporating 100, 500 and 1000 μL of poly(propylene imine) (PPI) dendrimer-protected silver nanoparticles (AgNPs) to create antibacterial-bolstered scaffolds using freeze-drying technique. Based on results, hAM/Gel2/S500 scaffold was identified as optimal specimen. It exhibited favorable properties, including an ultimate tensile strength of 16 kPa, an elastic modulus of 26.66 kPa, an elongation at break of 59.60%, an average pore size of 490 μm and a porosity of 52.93%. *In vitro* degradation indicated that degradation rate of the scaffold was 30% lower on the 1st day and 20% higher on the 21st day compared to commercial ChitoHeal dressing. It also demonstrated higher water absorbance of 100 and 139% at 1 and 48 hours, respectively, compared to ChitoHeal dressing. Additionally, uniform distribution of AgNPs throughout the scaffold and their release from 2.30 μg mL^{-1} on the 1st day to 10.40 μg mL^{-1} by the 3rd day, resulted in an elevated inhibition zone against *S. aureus* and *E. coli*. Finally, all antibacterial-bolstered scaffolds exhibited 85–89% cell viability after 24 hours and 80–83% after 72 hours. Consequently, hAM/Gel2/S500 scaffold showed promising results for application in wound healing.

Received 11th November 2024
Accepted 12th February 2025

DOI: 10.1039/d4ra08014a

rsc.li/rsc-advances

1. Introduction

The skin is the largest organ in the human body, with a surface area of approximately 1.5 to 1.8 m^2 and a thickness ranging from 0.5 (in the lower eyelid) to 15 mm (in the foot sole) in healthy adult. Its volume could vary from 7500 to 27 000 mm^3, reflecting its diverse physiological functions, which include mechanistic, energetic, metabolic and immunological roles.[1] In fact, skin creates a safety barrier against pathogens and defends the human body from external chemical, mechanical or physical insults. Skin loss could occur for various reasons, such as thermal trauma, genetic disorders, chronic wounds, burns or even surgical interventions.[2] Skin grafts are the most common approach in the treatment of chronic wounds.[3] However, in the case of deep or large wounds or extensive severe burns, due to low immunogenicity and the limited availability of donor skin, skin grafts often fail to provide complete recovery, rendering them unsuitable for widespread use.[4] With the advent of skin tissue engineering, the therapeutic potential for healing chronic wounds has significantly developed, as this advanced strategy aims to fabricate skin substitutes that act as bioactive wound dressings, facilitating wound healing rather than simply covering it.[5]

Human amniotic membrane (hAM), the innermost portion of the fetal membranes, is a biological tissue that surrounds the fetus in the mother's womb and has been applied as a biological scaffold in wound care.[6,7] It consists of three main layers: an epithelial monolayer that is separated from the stroma layer by a basement membrane.[8,9] The basement membrane is composed of various extracellular matrix components, such as different types of collagen, elastin, laminin, fibronectin, vitronectin and glycosaminoglycans. Additionally, it contains natural inhibitors and is rich in biologically active factors, including cytokines and growth factors, which have been shown to be promote wound healing and tissue regeneration.[10] Moreover, hAM exhibited a range of beneficial properties, including

[a]*Biomedical Engineering Department, Amirkabir University of Technology (Tehran Polytechnic), Tehran, Iran. E-mail: atefeh.solouk@aut.ac.ir*

[b]*New Technologies Research Center (NTRC), Amirkabir University of Technology (Tehran Polytechnic), Tehran, Iran. E-mail: haghbin@aut.ac.ir*

[c]*Department of Textile Engineering, Amirkabir University of Technology (Polytechnic Tehran), Tehran, Iran*

anti-inflammatory, anti-microbial, anti-fibrotic, anti-scarring, non-immunogenic, non-tumorigenic and bacteriostatic effects, as well as enhanced epithelialization.[11] Despite all these excellent properties, hAM has limited clinical use for wounds of varying dimensions due to three main limitations. First, its poor mechanical and handling characteristics hinder effective application.[12] Second, it has been observed that neither fresh nor acellularized hAM exhibits potent bactericidal activity against multidrug-resistant (MDR) bacterial strains.[13] This highlights the need for alternative treatment strategies to effectively address such infections.[14–20] Finally, the limited accessibility of fresh hAM due to its short shelf life has led to the development of various preservation methods, such as cryopreservation in liquid nitrogen,[17] which reduces its bactericidal properties after each cycle of cryopreservation.[20]

The poor mechanical and handling characteristics could be addressed by reinforcement with electrospun nanofibers that enhance its mechanical and handling properties.[21] For instance, gelatine (Gel) nanofibers have been successfully applied to construct a composite membrane through interfacial bonding to address the issues of the fragile nature and rapid degradation rate of decellularized hAM.[22] Gel is a natural mimic of the extracellular matrix found in human tissues and organs. The properties of Gel that have attracted the attention of most biomaterial researchers include excellent biocompatibility, good biodegradability, cell interactivity, non-immunogenicity, as well as its excellent processability, ready availability and cost-effectiveness.[23]

The insufficient protection against infections caused by MDR bacteria, along with the reduced bactericidal properties after each cycle of cryopreservation, could be addressed through antibacterial modification. One notable approach to combat bacteria and prevent wound infection is the incorporation of antimicrobial noble metals, with silver being the most popular choice.[24] Silver nanoparticles (AgNPs) have been widely used in medical devices due to their high biocidal activity against a broad spectrum of microbes and organisms. Specifically, AgNPs could serve as an effective antibacterial agent targeting *Pseudomonas aeruginosa* (*P. aeruginosa*).[25] Additionally, AgNPs exhibit lower toxicity to human cells compared to other metallic elements, making them a safer option for therapeutic applications. Their cost-effectiveness further enhances their appeal, allowing for widespread use in various medical and healthcare settings.[26] There are various methods to synthesize AgNPs,[27] including the dendritic-assisted method.[28,29]

Among various dendritic materials, those that are amine-terminated, such as poly(amidoamine) (PAMAM) and poly(propylene imine) (PPI) dendrimers, attract significant attention. PPI dendrimers have become one of the most popular polymers in biomedical engineering applications due to their spherical structure and high density of functional end groups. Furthermore, PPI dendrimers exhibit potent antibacterial properties due to their terminal amine groups, without inducing bacterial resistance.[20,30–37]

In this study, we explored the innovative combination of cryopreserved hAM with Gel and utilized dendrimer-protected AgNPs to develop an antibacterial biological scaffold tailored for the repair of partial and full-thickness wounds. Gel, renowned for its enzymatic biodegradability and biocompatibility in physiological environments, is used to enhance the mechanical and handling properties of the hAM. Furthermore, Gel serves as an ideal matrix due to its denatured collagen composition, which closely resembles the natural components of hAM. To counteract the reduction in antibacterial properties from cryopreserved hAM and to achieve sufficient protection against infections caused by MDR bacteria, the scaffold was fortified with AgNPs synthesized *via in situ* formation on PPI dendrimers, thereby enhancing its antibacterial efficacy.

2. Materials and methods

2.1. Materials

Commercial hAM was provided by Iranian Tissue Products Co., Iran. Gel, pepsin enzyme (obtained from porcine gastric mucosa), tetrahydrofuran ($M_w = 72.11$ g mol^{-1}), phosphate-buffered saline (PBS) tablet, HA ($M_w = 36.46$ g mol^{-1}), glutaraldehyde (GA) and glycine were purchased from Merck, Germany. The second generation of PPI (G2, $M_w = 773.28$ g mol^{-1}) was purchased from SyMo-Chem Co., Netherlands. Silver nitrate ($AgNO_3$) solution (0.1 M) was obtained from Titrachem Co., Iran. Sodium borohydride ($M_w = 37.83$ g mol^{-1}) was bought from Alpha Co., India. Ultrapure water was acquired from Dacell, Korea. L929 mouse fibroblast cells were obtained from National Cell Bank, Pasteur Institute, Iran. *Staphylococcus aureus* (*S. aureus*, ATCC 29213) and *Escherichia coli* (*E. coli*, ATCC 25922) strains were obtained from the Pathobiological Laboratory of Lashgarak, Iran. Commercial ChitoHeal foam dressing, which was used as the control in the test for morphological, mechanical, porosity and pore size, *in vitro* degradation and equilibrium water absorbance (EWA), was purchased from Chitotech Co., Iran. Commercial AGICOAT silver nanocrystalline dressing, which was used as the positive control in the disc diffusion antibacterial test, purchased from Emad Pharmaceutical Co., Iran. All the chemical substances were used without any refinement.

2.2. Synthesize AgNPs using PPI dendrimer-assistance

AgNPs were synthesized using dendrimer-assistance nanoparticle formation, where PPI dendrimers were employed as stabilizers. First, the PPI dendrimers were dissolved in tetrahydrofuran (THF) with a concentration of 1 mg mL^{-1}. Secondly, sodium hydroxide solution (20 mM) as a reducing agent was prepared by using ultrapure water (18 MΩ cm). In the next step, aqueous $AgNO_3$ (0.1 M) was added to the PPI dendrimers in a volume ratio of 1 : 1. Simultaneously, all mixtures were stirred vigorously for approximately 1 hour under the ambient atmosphere. Additionally, 15 μL of reducing agent was added to 5 mL of the $AgNO_3$/PPI solution to create AgNPs stabilized by PPI dendrimers.[28,38] Finally, the clear orange colour of the $AgNO_3$/PPI solution confirmed the production of AgNPs at a concentration of 100 ppm. In fact, metal ions that exhibit an affinity for amines are effectively adsorbed, primarily driven by mechanisms such as covalent bond formation, electrostatic interactions, complexation reactions, or a combination of these forces within PAMAM and PPI

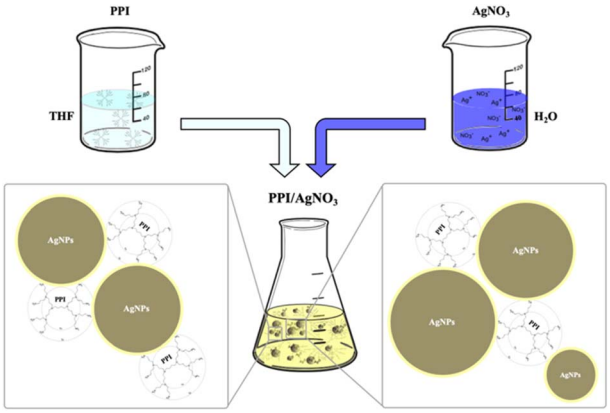

Fig. 1 Schematic of AgNPs synthesized using PPI dendrimer-assistance, illustrating how PPI and its surface amine groups act as stabilizing agents.

dendrimers.[39] As illustrated in Fig. 1, which presents a schematic of AgNPs synthesized using PPI dendrimer-assistance, dendrimers could form interdendrimer complexes that lead to the formation of larger metal nanoclusters. These nanoclusters are protected by the exterior amine groups, which provide stabilizing activity. Moreover, the amine-terminated functional groups in PPI dendrimers also enhance of the reducing agent activity.[40]

2.3. Preparation of hAM/Gel blend scaffold (mechanical-reinforced scaffolds)

To achieve the desired composition of the hAM and Gel blend sponge, four different formulations were prepared. First, 1.5% w/v fragmentary hAM was dissolved in 0.1 M hydrochloric acid (HCL) and 1 mg mL^{-1} pepsin enzyme by stirring for 60 hours at room temperature (hAM solution). Second, aqueous solutions of 2, 4, 6 and 8% w/v Gel powder were prepared by stirring for about 30 minutes at 45 °C (Gel solutions). Third, 2 mL of hAM solution was added to 10 mL of each Gel solution to create a total of 12 mL of hAM/Gel constituent solutions (hAM/Gel solution). Next, the solutions were stirred and poured into four sealed vessels, then kept in the refrigerator for 15 minutes to provide a homogeneous gel phase. Afterward, the gels were kept in a freezer at −85 °C for 24 hours. The obtained freeze-gels were then freeze-dried for 24 hours to create spongy scaffolds. GA vapor was used for cross-linking the scaffolds and enhancing their mechanical properties.[33,36,41] This procedure was performed in a sealed vacuum desiccator with 2 mL of 25% GA solution for 24 hours at 25 °C. Subsequently, the residual GA in the scaffold structure was neutralized with a 1 M glycine solution for 1–3 hours. Following this, the scaffolds were washed three times with PBS to eliminate any traces of glycine.[33]

2.4. Preparation of antibacterial hAM/Gel hybrid scaffold (antibacterial-bolstered scaffolds)

To enhance the bactericidal properties of the mechanical-reinforced scaffolds, various concentrations of PPI/AgNPs solution (100, 500 and 1000 μL) were added to the hAM/Gel solution containing 2% w/v of Gel. After stirring the solutions, the homogenized solutions were freeze-dried as previously described. Table 1 presents the specimen codes, and a schematic representation of the different steps of the work is shown in Fig. 2.

2.5. Characterization

2.5.1. Morphological analysis. To characterize the morphology of AgNPs, 1 μL of the PPI/AgNPs solution was diluted with distilled water, dried on aluminium foil, and analysed using field emission-scanning electron microscope (FE-SEM, MIRA3 TESCAN). Furthermore, the morphologies of commercial hAM, plain hAM, hAM/Gel and ChitoHeal scaffolds were observed using scanning electron microscope (SEM, Seron Technologies, AIS2300C). A thin gold layer was coated onto all the specimens before imaging.

2.5.2. Ultraviolet-visible spectrophotometry analysis. To characterize the AgNPs, the PPI/AgNPs solution was analysed ultraviolet-visible (UV-vis) spectroscopy (PerkinElmer, Lambda 950) in the range of 325 to 485 nm, which corresponds to the absorption peak of AgNPs.

2.5.3. Dynamic light scattering analysis. To characterize the size of AgNPs, the PPI/AgNPs solution was analysed using dynamic light scattering (DLS, Cordouan Tech, VASCO 2).

2.5.4. Mechanical properties. Elongation at break and tensile strength of the hAM/Gel and ChitoHeal scaffolds were measured in a wet state. The procedure of the experiment was as follows: first, the specimens were prepared with dimension of 5 × 2 × 0.3 cm. The two terminals of the tensile specimens were then fixed in a specific clamp. Next, elongation at break and tensile strength of the scaffolds were measured using a load cell of 50 N and the crosshead speed of 1 mm min^{-1} at ambient temperature. The results were reported as the average of three measurements for each specimen.

2.5.5. Porosity and pore size analysis. The total porosity of the hAM/Gel and ChitoHeal scaffolds was measured by the liquid displacement method.[42] In this method, scaffolds of known weight were placed in a liquid that permeates through the scaffold without dissolving it. Absolute ethanol, with a density of ρ_e, served as the displacement liquid because it is a nonpolar solvent that does not interfere with the Gel in the hAM/Gel scaffolds or with chitosan in the ChitoHeal scaffold,[43–45] thereby preventing any swelling or shrinkage the matrix. Firstly, the specimens were weighed before immersion in ethanol (W_s). Ethanol was then poured into each vial, and the vials containing ethanol were weighed (W_1). Afterwards, the specimens were placed in the filled vials and kept in the refrigerator for 24 hours at 4 °C. Next, the vials containing ethanol and specimens were weighed (W_2), after which the specimens were removed. Finally, the vials containing ethanol were weighed once more (W_3). The porosity of the scaffolds was calculated using eqn (1)–(3), where V_p and V_s represent the total volume of the pores and volume of the scaffold, respectively. Additionally, the pore size of scaffolds was estimated using ImageJ analysis software.

$$\text{Porosity}(\%) = \frac{V_p}{V_p + V_s} \times 100 \quad (1)$$

Table 1 Specifications of specimens and their codes

Treatment	Specimen code	hAM content (% w/v)	Gel content (% w/v)	PPI/AgNPs content (μL)
Plain scaffold	Plain hAM	1.5	—	—
Mechanical-reinforced scaffolds	hAM/Gel2	1.5	2	—
	hAM/Gel4	1.5	4	—
	hAM/Gel6	1.5	6	—
	hAM/Gel8	1.5	8	—
Antibacterial-bolstered scaffolds	hAM/Gel2/S100	1.5	2	100
	hAM/Gel2/S500	1.5	2	500
	hAM/Gel2/S1000	1.5	2	1000

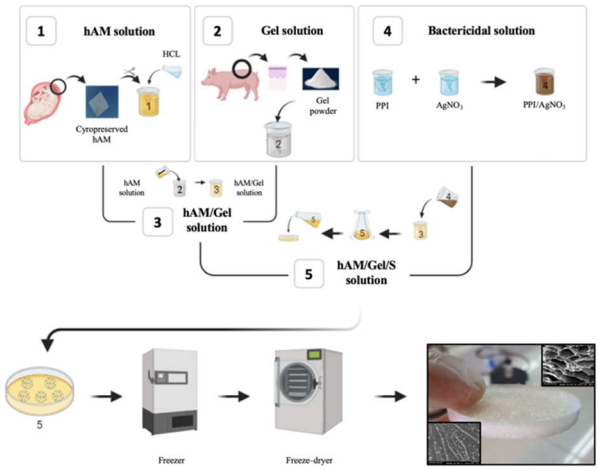

Fig. 2 Schematic of the different steps of the work.

$$V_p = \frac{W_2 - W_3 - W_s}{\rho_e} \quad (2)$$

$$V_s = \frac{W_1 - W_2 + W_s}{\rho_e} \quad (3)$$

2.5.6. *In vitro* degradation study. To evaluate the degradation rate of the hAM/Gel and ChitoHeal scaffolds, uniform specimens were first weighed. The specimens were then immersed in PBS at pH = 7.4 and 37 °C. Specimens were removed after 1, 3, 7, 14 and 21 days, washed with deionized water to remove adsorbed ions from the surface, and subsequently freeze-dried again. The initial weight (W_i) and final weight (W_f) of the dry specimens were recorded. Finally, the degradation of the scaffolds was calculated using eqn (4).[46] This test was repeated three times for each specimen.

$$\text{Degradation}(\%) = \frac{W_i - W_f}{W_i} \times 100 \quad (4)$$

Furthermore, the morphology of the cross-section and surface structure of the hAM/Gel scaffolds after 7 days of incubation at 37 °C was examined using the same SEM. The cross-sectioned scaffolds were prepared by fracturing them in liquid nitrogen.

2.5.7. Equilibrium water absorbance study. The hAM/Gel and ChitoHeal scaffolds were cut into small, equal segments and immersed in PBS at pH = 7.4 and 37 °C. Next, the specimens were removed at predetermined intervals (1, 2, 3, 4, 8, 12, 24 and 48 hours), and any adsorbed water on the surface was blotted off with filter paper before they were immediately weighed. The EWA percentage of EWA was calculated using eqn (5), where W_w and W_d represent the wet and dry weight of the specimens, respectively.[46]

$$\text{EWA}(\%) = \frac{W_w - W_d}{W_d} \times 100 \quad (5)$$

2.5.8. Fourier transform infrared analysis. Fourier transform infrared (FTIR, Thermo Scientific IS10) was conducted to identify the presence of hAM and Gel in the plain hAM and hAM/Gel scaffolds, as well as to analyse the bactericidal solution in the hAM/Gel2/S scaffolds. Spectra were collected over a wavelength range of 4000 to 400 cm^{-1}.

2.5.9. *In vitro* release behaviour of AgNPs. The distribution and dispersion of AgNPs within the hAM/Gel/S scaffolds were analysed using the same SEM. Furthermore, the amount of AgNPs released from the hAM/Gel2/S scaffolds was analysed using the same UV vis spectroscopy. Firstly, a UV calibration standard line for AgNPs was established by preparing serial dilutions of various concentrations of the antibacterial solution based on the absorption values at 400 nm, which corresponds to the absorption peak of AgNPs. Secondly, to determine the amount of AgNPs released by each specimen, hAM/Gel2/S scaffolds were cut into 1 × 1 × 3 cm pieces and placed in PBS. They were then incubated for one to three days to simulate the wound environment. Finally, the solutions containing the degradation products of the specimens were analysed. Based on the Beer–Lambert law, the concentration of AgNPs in the degradation products was calculated for each specimen, where A is absorbance, ε is the molar absorptivity of the absorbing species, b is the path length and c is the concentration of the absorbing species (eqn (6)).

$$A = \varepsilon bc \quad (6)$$

2.5.10. Antibacterial activity. To evaluate the antibacterial properties of the hAM/Gel2 and hAM/Gel2/S scaffolds, the disc

diffusion antibacterial test was employed against *S. aureus* and *E. coli*. Each specimen was cut into pieces measuring 1 × 1 cm and sterilized for 20 minutes using 70% ethanol. Both bacterial strains were cultured in 10 mL of sterilized Luria–Bertani (LB) medium at 37 °C for 18–24 hours (repeated three times). Following this, 1.5 mL of culture medium was centrifuged at 1000 rpm for 1 minute; the supernatant was removed, and the pellet was resuspended in 1 mL of sterilized LB medium. To prepare a bacterial suspension at a 0.5 McFarland concentration (1.5×10^8 CFU mL^{-1}), an additional 4.5 mL of LB medium was added. The absorbance of the suspensions was measured at 625 nm to ensure it fell within the range of 0.08 to 0.10 for the 0.5 McFarland standard. Subsequently, 500 μL of the adjusted suspension was added to separate containers containing 4.5 mL of LB medium, which were then incubated at 37 °C with shaking at 200 rpm for 24 hours. From each specimen, 100 μL was taken and diluted with 900 μL of saline to determine the colony-forming units of the bacteria. Eight suspensions consisting of this main solution were spread on LB agar plates and incubated at 37 °C for 24 hours. For preparing the nutrient medium, 5 mL was poured into two 15 mL Petri dishes. Then, 1 mL of inoculum from the glycerol stock of each bacterial strains was added and incubated at 37 °C for 10 hours. Nutrient agar was prepared and sterilized by autoclaving at 121 °C for 15 minutes before inoculated each Petri dish using the spread plate procedure 100 μL was pipetted onto each and spread evenly with a sterile L-rod. Finally, the specimens were placed onto the Petri dishes, which were incubated at 37 °C for another 24 hours.[47,48] After labelling, the inhibition zones of all specimens were measured from the edge of each specimen to the edge of the zone of inhibition, where no bacterial growth was observed, using ImageJ analysis software.

2.5.11. Biological evaluation. The Biological properties of the scaffolds were explored through cell viability and morphology assays by assessing the interaction of mouse fibroblast cells (L929, NCBI C161) with the specimens. The Roswell Park Memorial Institute (RPMI)-1640 was used as the culture medium for fibroblast cells. (I) Cell Viability Study: Based on the International Organization for Standardization (ISO 10993-5), an *in vitro* indirect contact cytotoxicity assay was performed on hAM/Gel2/S scaffolds to assess cell viability. This test measured cell viability by converting yellowish MTT into purple formazan, indicating metabolic activity; thus, the reduction of MTT into formazan reflects the level of cell metabolism. Commercial AGICOAT was used as the positive control, while plain hAM served as the negative control. The specimens were incubated in the medium at 37 °C for 1 and 3 days, with an extraction proportion of 6 cm^2 mL^{-1} after being sterilized with 70% ethanol. The specimen extracts were then collected and used for the MTT assay. (I) Cell viability study: Based on the International Organization for Standardization (ISO 10993-5), an *in vitro* indirect contact cytotoxicity assay was performed on hAM/Gel2/S scaffolds to assess cell viability. This test measured cell viability by converting yellowish MTT into purple formazan, which indicates metabolic activity; thus, the reduction of MTT into formazan reflects the level of cell metabolism. Commercial AGICOAT was used as the positive control, while plain hAM served as the negative control. The specimens were incubated in the medium at 37 °C for 1 and 3 days, with an extraction proportion of 6 cm^2 mL^{-1} after being sterilized with 70% ethanol. The specimen extracts then collected and used for the MTT assay. The cells were seeded in a 96-well plate at a density of 1×10^4 cell per well. Each well received 100 μL of culture medium containing 10% FBS and was incubated for 24 hours. The medium was then replaced with 100 μL of specimen extracts mixed with FBS in a 90 : 10 (v/v) ratio. After another 24 hours, the medium was removed, and the wells were washed with PBS. Subsequently, 0.5 mg mL^{-1} MTT reagent in PBS was added to each well, and the plate was incubated at 37 °C for 4 hours. After removing the MTT solution, the formazan crystals were dissolved in isopropyl alcohol in each well. Optical absorbance measurements were performed at 570 nm using an ELISA microplate reader (STAT FAX 2100, USA). The cell viability of the scaffolds was normalized to that of the control specimen (the plate floor) and calculated using eqn (7).[49]

$$\text{Cell viability}(\%) = \frac{\text{Average optical density of membrane}}{\text{Average optical density of control}} \times 100 \quad (7)$$

(II) Cell morphology study: the sterilized hAM/Gel2/S500 specimen was placed in 12-well plates. Subsequently, the cells were seeded onto the specimen at a density of 1×10^4 cells per well and cultured in a complete medium composed of RPMI-1640 culture medium supplemented with 1% antibiotic penicillin/streptomycin and 10% v/v FBS in a humidified incubator at 37 °C and 5% CO_2. The culture medium was exchanged every two days. After 24 hours of cell seeding, the cell-containing specimen was washed twice with PBS and then fixed using a 2.5% GA solution. The fixed cells were dehydrated in graded concentrations of ethanol (50, 60, 70, 80, 90 and 100% v/v). Cell attachment and morphology on the surface of the scaffold were studied by the same SEM.

2.6. Statistical analysis

Using the SPSS software, all results were reported as means ± standard deviations (SD), and a p-value of ≤ 0.05 was considered statistically significant. Moreover, a one-way analysis of variance (ANOVA) was performed to evaluate the differences between groups.

3. Results and discussion

3.1. Characterization of AgNPs

The data characterization of the synthesized AgNPs is presented in Fig. 3. The FE-SEM image (Fig. 3(a)) illustrates a uniform spherical morphology and consistent size of the AgNPs. The UV-vis spectrophotometry analysis (Fig. 3(b)) reveals a distinct absorbance peak between 385 and 425 nm, which is a defining feature of AgNPs.[28,40,50] This peak is indicative of the surface plasmon resonance (SPR) phenomenon, which is significantly influenced by the size of the nanoparticles. In fact, the position

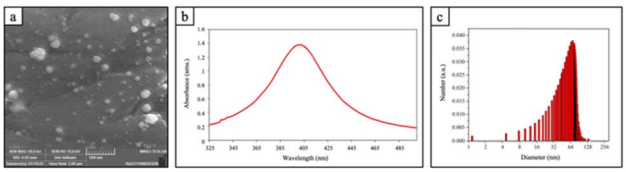

Fig. 3 Characterization of AgNPs by (a) FE-SEM, (b) UV-vis and (c) DLS.

of the SPR could be finely tuned by adjusting the size of AgNPs, typically ranging from 60 to 100 nm. Furthermore, by varying the solution concentration during the growth phase, a red shift in the SPR wavelength has been observed, ranging from 395 to 450 nm.[51] The presence of a single dipole SPR peak in the extinction spectra validate the spherical morphology of the synthesized nanoparticles, indicating a symmetric shape of the resulting nanoparticles.[52,53] Finally, the DLS results (Fig. 3(c)) indicate an average particle size of 69 nm. This measurement aligns well with the expectations derived from UV-vis spectrophotometry, which shows an absorbance peak at 400 nm for the AgNPs.

3.2. Characterization of the scaffolds

3.2.1. Morphological analysis. The SEM images of the commercial hAM, plain hAM, hAM/Gel and ChitoHeal scaffolds are shown in Fig. 4. According to Fig. 4(a), commercial hAM did not show any porosity, which is a crucial feature for proper cell nutrition and infiltration.[24,54] Furthermore, it was unable to absorb exudate from wounds due to its lack of an adequate porous structure, which is essential for effective absorption.[55] To address this issue, a sponge-like porous scaffold was made using commercial hAM, which is henceforth called plain hAM (Fig. 4(b)). However, a large number of hAM sheets were required to yield the porous scaffold, and also the porosities were not uniform. Therefore, Gel served as a blend component in four different ratios, and the structures of the blended scaffolds (hAM/Gel) with 2, 4, 6 and 8% Gel are presented in Fig. 4(c)–(f), respectively. Interestingly, addition of Gel to the plain hAM scaffold resulted in improved pore size distribution, and greater homogeneity by increasing Gel content up to 4%, and then reduced at 6 and 8%, which aligns with the results of previous studies.[56] As a result, the hAM/Gel scaffolds containing 2 and 4% w/v Gel exhibited better pore size distribution compared to the other hAM/Gel scaffolds. Finally, the SEM image of the ChitoHeal scaffold, as a commercial product, is shown in Fig. 4(g).

3.2.2. Mechanical properties. The elastic modulus, ultimate tensile strength and elongation at break of the hAM/Gel and ChitoHeal scaffolds are reported in Table 2. The plain hAM scaffold was so brittle that handling it and performing tensile strength tests were not possible. Addition of Gel to the blended scaffold improved handling, and significantly enhanced the mechanical properties,[57] increasing the ultimate tensile strength from 16 to 34 kPa, increasing the elastic modulus from 26.66 to 90.00 kPa, but decreasing the elongation at break from 59.60 to 42.39%. In fact, ultimate tensile strength

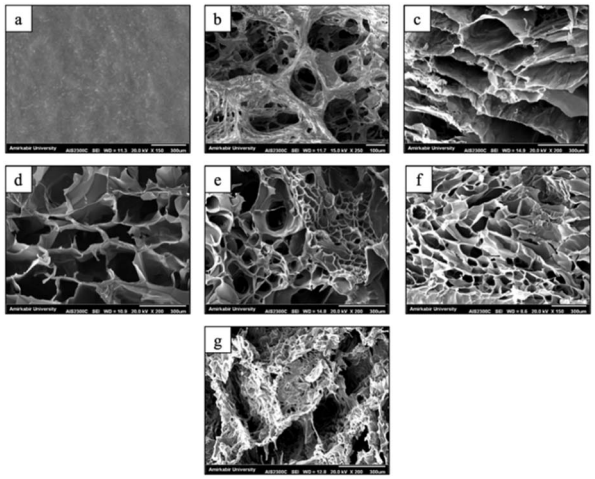

Fig. 4 SEM images of (a) commercial hAM, (b) plain hAM, (c) hAM/Gel2, (d) hAM/Gel4, (e) hAM/Gel6, (f) hAM/Gel8 and (g) ChitoHeal.

and elastic modulus of hAM/Gel2 were the lowest compared to the other hAM/Gel scaffolds; however, it exhibited maximum elongation at break and flexibility. Increasing the Gel content results in a higher concentration of amino functional groups, which further facilitates crosslinking reactions. It is common in experimental works to harden Gel through crosslinking by aldehydes with low molecular weight, such as formaldehyde and GA.[58] Since the crosslinking process was conducted using vaporized GA on the scaffolds, crosslinking of the ε-amino, and formyl groups present in hydroxylysine, and lysine remnants is mainly performed by Schiff's base formation through condensation. Gel crosslinking using GA causes the formation of short aliphatic sections between Gel polymeric chains. As a result, a higher Gel content in the hAM/Gel scaffolds, leads to an increased formation of amino groups throughout the entire scaffold structure. This may increase both physical and chemical crosslinking, which leads to an increased ultimate tensile strength and elastic modulus, but a decreased flexibility. However, enhancement inadvertently compromises the inherent bactericidal capabilities of the scaffolds, as indicated in previous studies.[33,41,59] It should be noted that the significant differences in the values of ultimate tensile strength and elastic modulus between hAM/Gel and commercial ChitoHeal arise from the fact that the hAM/Gel scaffolds are hydrogel-like, whereas the ChitoHeal is a rigid foam.

3.2.3. Porosity and pore size analysis. Average pore size and porosity of the hAM/Gel and ChitoHeal scaffolds are reported in Table 3. According to the values, porosity of hAM/Gel scaffolds ranged from 52.50 to 56.17%, with no significant variation (p-value > 0.05). In other words, increasing the Gel content in the hAM/Gel scaffolds did not result in a significant change in porosity. However, a significant decrease (p-value ≤ 0.05) in the average pore size of the hAM/Gel scaffolds was observed, from 490 μm (hAM/Gel2) to 110 μm (hAM/Gel8) as more lamellar structure layers were created. In fact, increasing the Gel content in the hAM/Gel scaffolds resulted in smaller and denser pores (Fig. 4(b)–(f)), which is consistent with the previous

Table 2 Mechanical properties of the hAM/Gel and ChitoHeal scaffolds

Specimen	Ultimate tensile strength (kPa)	Elastic modulus (kPa)	Elongation at break (%)
hAM/Gel2	16 ± 2.10	26.66 ± 0.94	59.60 ± 1.40
hAM/Gel4	23 ± 2.20	56.66 ± 1.25	44.78 ± 1.30
hAM/Gel6	25 ± 2.40	73.33 ± 1.25	46.22 ± 1.50
hAM/Gel8	34 ± 2.20	90.00 ± 1.43	42.39 ± 1.80
ChitoHeal	360 ± 10.0	1260.00 ± 22.34	33.96 ± 1.40

observations.[60] A possible reason for this effect might be the enhanced hydrophilicity of the polymeric blend solution after increasing the Gel concentration. Additionally, this effect resulted in a higher water absorption, and a decrease in trapped water, which helps prevent the formation of ice crystals. Consequently, a reduction in pore size occurred. In fact, the capacity for water adsorption is grater in porous scaffolds with effective distribution than in non-porous ones due to the increased void space for capillary-adsorbed water. This characteristic hinders fluid accumulation in defective areas by adsorbing wound exudates. Furthermore, porosity in the structure of the scaffolds may promote cell nutrition, and increase the effective surface area for cell attachment.[61] As a result, the hAM/Gel scaffold containing 2% w/v Gel, which exhibits the highest average pore size and sparse pore structure compared to other hAM/Gel scaffolds, could be more efficient in adsorbing wound exudates and facilitating cell attachment. It should be noted that while the average pore size of the ChitoHeal is similar to that of the hAM/Gel scaffolds containing 2% and 4% Gel, porosity of the ChitoHeal is significantly lower than that of all the hAM/Gel scaffolds.

3.2.4. *In vitro* degradation study. Fig. 5 illustrates the weight loss percentage of hAM/Gel and ChitoHeal scaffolds after various soaking periods of 1, 3, 7, 14 and 21 days. Regarding the values, increasing the Gel content in the hAM/Gel scaffolds enhanced their degradation rate, which aligns with the results of previous studies.[62] For instance, increasing the Gel content from 2 to 8% resulted in a significant boost in the degradation rate, which increased from 10.07 to 33.06% on the 1st day, from 37.58 to 48.29% on the 3rd day, and 58.39 to 80.07% on the 7th day of the degradation period (p-value ≤ 0.05). After the 7th day of the degradation period, only insignificant differences were observed among the hAM/Gel scaffolds (p-value > 0.05). It should be noted that the degradation rate did not change due to the presence of hAM in the hAM/Gel scaffolds. In other words, the Gel/hAM ratio plays a crucial role due to hAM's lower degradability compared to Gel, even though it may contribute to a controlling the degradation of the hAM/Gel scaffolds in the early days.

Fig. 6 illustrates the cross-section and surface structure of the degradation morphology in hAM/Gel scaffolds following incubation for 7 days. As shown in Fig. 6(a)–(d), which shows the cross-section of the hAM/Gel scaffolds, the hAM/Gel2 scaffold retains bulk porosity during degradation. In contrast, scaffolds with higher Gel content (4, 6 and 8%) exhibit a reduction in bulk porosity. In Fig. 6(e)–(h), which shows the surface, it can be observed that, similar to bulk porosity, a higher Gel content (4, 6 and 8%) in the scaffold results in a reduction in surface porosity. The bulk and surface porosity are crucial, as these pores facilitate air supply during the wound healing process. Therefore, it is essential for the scaffolds to maintain porosity throughout degradation. The degradation is also crucial because it may control the release of AgNPs. As a result, the hAM/Gel scaffold containing 2% w/v Gel, which exhibits the highest bulk and surface porosity during degradation compared to the other hAM/Gel scaffolds, could be more efficient in facilitating air supply during the wound healing process while also controlling the release of AgNPs.

3.2.5. Equilibrium water absorbance study. The EWA of hAM/Gel and ChitoHeal scaffolds is presented in Fig. 7. The results demonstrate that all scaffolds exhibited water uptake ranging from 102 to 1112% on the 1st day of the measurement. On the 2nd day, EWA showed a slight significant increase (p-value ≤ 0.05) for hAM/Gel2, while it significantly diminished for hAM/Gel4 (p-value ≤ 0.05). For all other scaffolds, EWA remained relatively unchanged on the 2nd day (p-value > 0.05).

Table 3 Pore size and porosity of the hAM/Gel and ChitoHeal scaffolds

Specimen	Average pore size (μm)	Porosity (%)
hAM/Gel2	490 ± 11	52.93 ± 4.13
hAM/Gel4	420 ± 20	52.50 ± 4.14
hAM/Gel6	210 ± 34	53.04 ± 2.41
hAM/Gel8	110 ± 10	56.17 ± 2.42
ChitoHeal	410 ± 21	31.54 ± 1.86

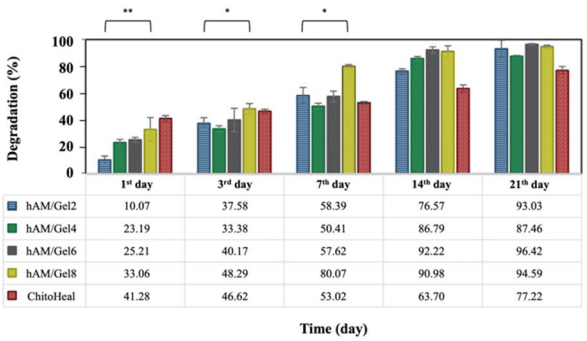

Fig. 5 Degradation of hAM/Gel and ChitoHeal scaffolds (* for p-value ≤ 0.05 and ** for p ≤ 0.005).

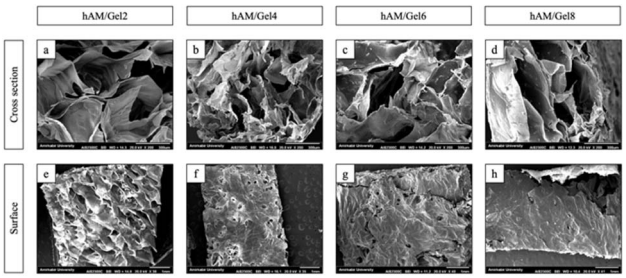

Fig. 6 SEM images of (a) degraded hAM/Gel2 (cross section), (b) degraded hAM/Gel4 (cross section), (c) degraded hAM/Gel6 (cross section), (d) degraded hAM/Gel8 (cross section), (e) degraded hAM/Gel2 (surface), (f) degraded hAM/Gel4 (surface), (g) degraded hAM/Gel6 (surface), (h) degraded hAM/Gel8 (surface).

The highly porous nature of the wound dressings could be useful for adsorbing a high volume of wound exudates; whereas, porosity affects EWA%.[46] Since Gel was used as a pore producer, it could be concluded that additional Gel in scaffolds results in a greater EWA%. However, this may not apply to all cases because mass loss is another effective parameter that must be considered. In fact, degradation plays a role in W_w, and it directly affects EWA%. W_w represents the sum of the weight gain due to water absorption, and weight loss due to degradation. Since the degradation of high-Gel content scaffolds is more pronounced in the early days, the W_w of high-Gel content scaffolds (6 and 8%) is less than W_w of low-Gel content scaffolds (2 and 4%). Consequently, the EWA% of low-Gels is greater than that of their high-Gels counterparts. As a result, the hAM/Gel scaffold containing 2% w/v Gel, which exhibits the highest EWA compared to the other hAM/Gel scaffolds, could be more efficient in adsorbing a high volume of wound exudates.

Based on the results of the morphological analysis, porosity and pore size analysis, *in vitro* degradation study and EWA study, the specimen containing 2% w/v Gel (hAM/Gel2) was identified as the optimal specimen among the hAM/Gel scaffolds. This designation is attributed to its superior pore size distribution, highest average pore size, greatest bulk and surface porosity during degradation and highest EWA. Consequently, the remaining characterizations were conducted using this specimen, incorporating it with 100 μL (hAM/Gel2/S100), 500 μL (hAM/Gel2/S500) and 1000 μL (hAM/Gel2/S1000) of PPI dendrimer-protected AgNPs.

3.2.6. Fourier transform infrared analysis. The FTIR spectra of plain hAM, hAM/Gel and hAM/Gel2/S scaffolds are displayed in Fig. 8. Based on Fig. 8(a), the FTIR spectra of plain hAM and hAM/Gel scaffolds shows peaks consistent with previous studies.[63] In the spectrum of plain hAM, there are the characteristic absorption bands at 2959, 1652, 1551, 1453, 1398, 1240, 1079 and 652 cm^{-1}. The absorption band at a frequency of 1600–1640 cm^{-1} is related to the amide I protein absorption band, predominantly attributed to the C=O stretching mode. Additionally, the peaks in the range of 1510–1560 cm^{-1} are attributed to the amide II protein absorption band, associated with C–N stretching and N–H bending modes. The absorption band within the ranges of 1210–1300 and 1070–1080 cm^{-1} are attributed not only to amide III protein but also to the phosphodiester group of nucleic acids, phospholipids and glycolipids. The absorption band attributed to amide III result from the interaction of N–H in plane-bending and C–N stretching modes, with some contributions from C=O bending vibrations and C–C stretching.[64] Proteins spectra are characterized by amide and carboxyl groups. A significant shift in the amide II band from 1550 to 1517 cm^{-1} correlates with collagen helix denaturation.[65] It should be noted that adding Gel (as denatured collagen) to the compound caused this shift. This alteration highlights an enhanced separation of the amide I and amide II bands at 1650 and 1550 cm^{-1}. In addition, the weaker peaks in the ranges of 1600–1640 cm^{-1}, related to C=O, and 1510–1560 cm^{-1} related to N–H, indicate that carboxyl and amine groups in hAM have reacted with amine and carboxyl groups in Gel, respectively. Furthermore, the peak at 2960 cm^{-1} may be attributed to the asymmetric stretching mode of the methyl (CH_3) group. Based on Fig. 8(b), it can be observed that adding more bactericidal solution to the hAM/Gel2 scaffold attenuates the peaks assigned to C=O and N–H. Specifically, the increase in the antibacterial solution in the compound causes an interaction of these amine groups with unreacted carboxyl groups in the compound due to the presence of amine terminal groups in the PPI dendrimers. Therefore, the related peaks were reduced.[63]

3.2.7. *In vitro* release behaviour of AgNPs. Fig. 9 shows the presence of AgNPs in the cross-section and surface structure of hAM/Gel2/S scaffolds. According to Fig. 9(a) and (d), which

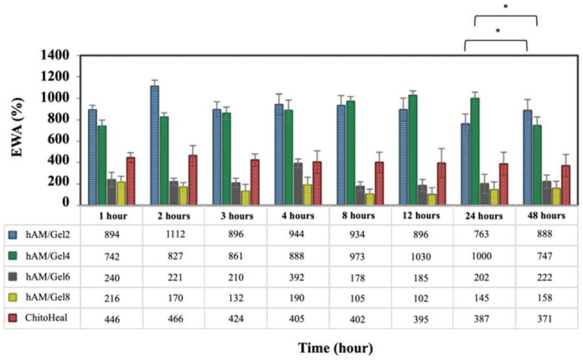

Fig. 7 EWA of hAM/Gel and ChitoHeal scaffolds (* for p-value ≤ 0.05).

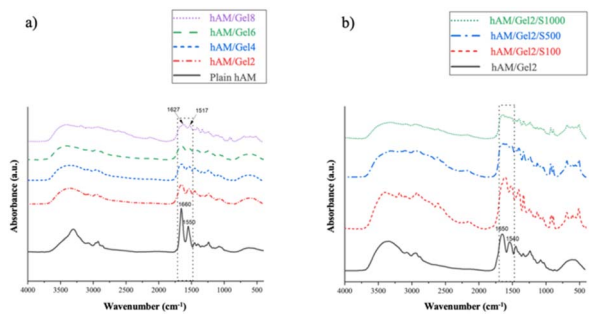

Fig. 8 FTIR spectra of (a) plain hAM and hAM/Gel scaffolds and (b) hAM/Gel2 and hAM/Gel2/S scaffolds.

display the cross-section and surface of hAM/Gel2/S100, respectively, the amount of AgNPs exposed in this scaffold is low. Additionally, Fig. 9(b) and (e), which illustrate the cross-section and surface of hAM/Gel2/S500, demonstrate that hAM/Gel2/S500 has an adequate amount and uniform distribution of AgNPs throughout the scaffold. Finally, Fig. 9(c) and (f), which show the cross-section and surface of hAM/Gel2/S1000, respectively, indicate that AgNPs are dense and agglomerated in the scaffold.

The amount of AgNPs released from the hAM/Gel2/S scaffolds in the wound-simulated area is shown in Table 4. The amounts of free AgNPs varied from 1.02 to 2.67 μg mL^{-1} on the 1st day, and from 2.23 to 12.19 μg mL^{-1} on the 3rd day across all hAM/Gel2/S scaffolds. The results of this assay indicate a consistent release of AgNPs upon contact with the body. In fact, high concentrations of AgNPs (greater than 44.0 μg mL^{-1}) could lead to rapid rupture of the cell membrane, resulting in cytotoxic effect.[66] However, since small amounts of AgNPs were used in the scaffold formulation, it is anticipated that the side effects of AgNPs in the wound area will be negligible. Therefore, it is expected that all hAM/Gel2/S scaffolds demonstrate an acceptable level of toxicity.

3.2.8. Antibacterial activity. Table 5 presents the calculated data on bacterial activity (inhibition zone) of Plain hAM, hAM/Gel2, hAM/Gel2/S and AGICOAT scaffolds against *S. aureus* and *E. coli*. Furthermore, Fig. 10 illustrates the results of the disc diffusion test for these scaffolds. First, it should be noted that due to the inherent antibacterial properties of hAM, plain hAM demonstrates significant bactericidal activity against both microorganisms, with inhibition zones measuring 8.30 mm for *S. aureus* and 11.18 mm for *E. coli*. However, due to the use of only 1.5% w/v of hAM in our scaffolds, it is expected that the antibacterial activities of the hAM/Gel and hAM/Gel/S scaffolds would be significantly lower. Bactericidal activity against the Gram-positive bacterium *S. aureus* is evident, with an inhibition zone of 2.98 mm observed in the scaffold free of AgNPs (hAM/Gel2). The antibacterial property of this scaffold is entirely attributed to hAM. Furthermore, hAM/Gel2/S100, hAM/Gel2/S500 and hAM/Gel2/S1000 exhibit enhanced bactericidal activities against *S. aureus*, with inhibition zones of 3.16 mm, 3.44 mm and 4.22 mm, respectively. In contrast, no antibacterial activity is observed in the scaffold free of AgNPs (hAM/Gel2) against the Gram-negative bacterium *E. coli*, as this bacterium possesses two membranes, making it more resilient against bactericidal agents. However, there is antibacterial activity against *E. coli* for hAM/Gel2/S100, hAM/Gel2/S500 and hAM/Gel2/S1000, with inhibition zones of 4.42 mm and 5.41 mm, respectively. Therefore, all the hAM/Gel2/S scaffolds demonstrate effective bactericidal activity against both microorganisms. Previous research indicates that hAM exhibits limited antibacterial activity against *E. coli*, *S. aureus* and *P. aeruginosa*, while showing no antibacterial activity against *Klebsiella pneumoniae* (*K. pneumoniae*).[13] Since the biologically-based bactericidal scaffolds fabricated in this study incorporate three different antibacterial components (AgNPs, PPI dendrimers and hAM) and show antibacterial effects against *E. coli* and *S. aureus*, we expect that these antibacterial effects could extend to *P. aeruginosa*. However, we could not extend these antibacterial effects to *K. pneumoniae*.

Table 4 The amount of AgNPs released from the hAM/Gel2/S scaffolds in the wound simulated area

Specimen	AgNPs amount at 1st day (μg mL^{-1})	AgNPs amount at 3rd day (μg mL^{-1})
hAM/Gel2/S100	1.02 ± 0.30	2.23 ± 0.35
hAM/Gel2/S500	2.30 ± 0.27	10.40 ± 0.46
hAM/Gel2/S1000	2.67 ± 0.39	12.19 ± 0.81

3.2.9. Biological evaluation. The MTT assay conducted on the plain hAM, hAM/Gel2/S and AGICOAT scaffolds is represented in Fig. 11. The results exhibited no toxic effects at 24 and 72 hours for both positive and negative controls. Moreover, all hAM/Gel2/S scaffolds showed 85–89% cell viability after 24 hours and 80–83% cell viability after 72 hours. After 72 hours, cell viability was reduced due to the increased release of AgNPs resulting from further degradation of the scaffolds. Therefore, the hAM/Gel2/S500 scaffold demonstrates better cell viability than the hAM/Gel2/S1000 scaffold. Furthermore, it should be noted that the difference in the cell viability values could also result from the cell-material surface interaction, which is influenced by numerous complicated factors such as surface charge, wettability, morphology, roughness, and free energy.[67]

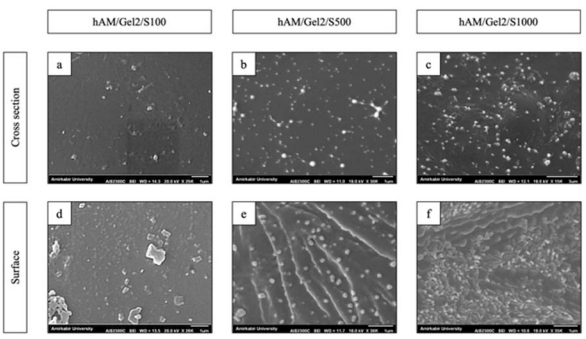

Fig. 9 SEM images of (a) AgNPs in hAM/Gel2/S100 (cross section), (b) AgNPs in hAM/Gel2/S500 (cross section), (c) AgNPs in hAM/Gel2/S1000 (cross section), (d) AgNPs in hAM/Gel2/S100 (surface), (e) AgNPs in hAM/Gel2/S500 (surface) and (f) AgNPs in hAM/Gel2/S1000 (surface).

Table 5 Inhibition zones of bacterial activity of plain hAM, hAM/Gel2, hAM/Gel/S and AGICOAT scaffolds against *S. aureus* and *E. coli*

	Inhibition zone (mm)	
Specimen	*S. aureus*	*E. coli*
Plain hAM	8.30 ± 0.42	11.18 ± 0.34
hAM/Gel2	2.98 ± 0.26	—
hAM/Gel/S100	3.16 ± 0.60	3.53 ± 0.53
hAM/Gel/S500	3.44 ± 0.15	4.42 ± 0.36
hAM/Gel/S1000	4.22 ± 0.22	5.41 ± 0.37
AGICOAT	1.67 ± 0.18	2.67 ± 0.58

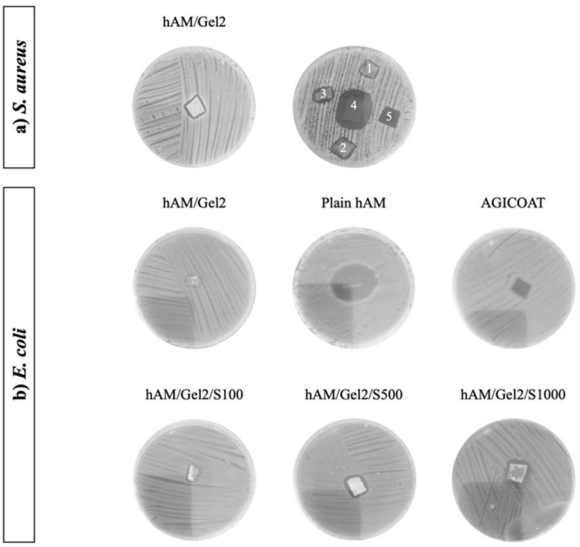

Fig. 10 Disc diffusion antibacterial test of plain hAM, hAM/Gel2, hAM/Gel2/S and AGICOAT scaffolds against (a) *S. aureus* and (b) *E. coli*. The numbers 1, 2, 3, 4 and 5 in section (a) correspond to hAM/Gel2/S100, hAM/Gel2/S500, hAM/Gel2/S1000, plain hAM and AGICOAT, respectively.

Based on the results of the antibacterial activity and biological evaluation, the specimen containing 2% w/v Gel and 500 μL of PPI dendrimer-protected AgNPs (hAM/Gel2/S500) was identified as the optimal specimens among the hAM/Gel2/S scaffolds. This designation is attributed to its uniform distribution of AgNPs throughout the scaffold, which demonstrates bactericidal activity against both microorganisms while maintaining the highest cell viability. Furthermore, in the realm of clinical scenarios, this scaffold could be competitive with ChitoHeal commercial dressing because it not only exhibits similar characteristics but also demonstrates superior properties such as enhanced antibacterial activity.

Finally, the fibroblast cell morphology from two different locations of hAM/Gel2/S500, identified as the optimum specimen, is shown in Fig. 12(a) and (b). This scaffold exhibits inherent properties that lead to improved cell adhesion. In fact, fibroblast cells were successfully attached to the surface of the

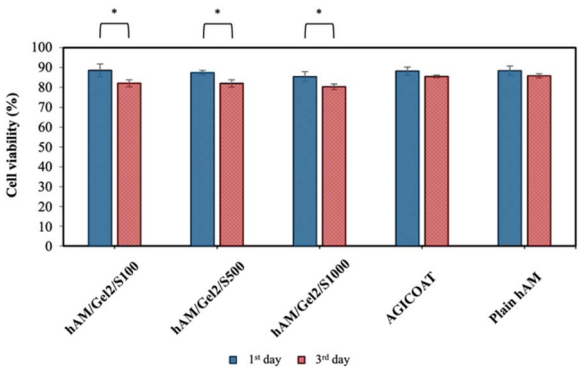

Fig. 11 Cell viability of plain hAM, hAM/Gel2/S and AGICOAT scaffolds on 1st day and 3rd day (* for p-value ≤ 0.05).

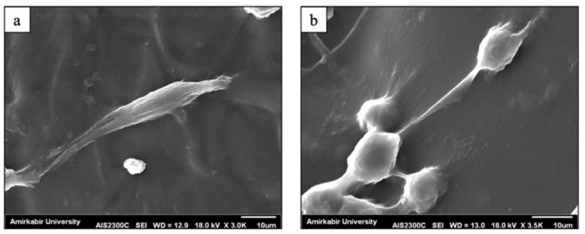

Fig. 12 (a and b) Fibroblast cell morphology from two different locations of hAM/Gel2/S500 as optimum scaffold.

scaffold, indicating a proper interaction between the scaffold and the cells. This finding aligns with the previous studies that demonstrated good adherence and viability of fibroblast cells on decellularized hAM.[68] Moreover, it has been noted that collagen accumulation occurs specifically at the front of the cell protrusions after fibroblasts adhesion.[69] The fibroblast protrusions depicted in this figure are the primary means by which fibroblast remodel their surrounding fibrous collagen matrices. Hence, hAM/Gel2/S500 scaffold may accelerate fibroblast adhesion compared to wounds without the scaffold, potentially leading to improved wound healing.[66]

4. Conclusions

In the present study, an effective skin regeneration scaffold was developed through a systematic approach that involved optimizing composition, enhancing antibacterial properties and evaluating scaffold performance. Initially, the optimization of hAM and Gel concentrations was performed. By mixing four different concentrations of Gel (2, 4, 6 and 8% w/v) with an equivalent amount of hAM solution (1.5% w/v), it was determined that the hAM/Gel2 scaffold exhibited uniform pore size, a high average pore size, excellent water absorbance and favourable degradability. Subsequently, the antibacterial properties of the hAM/Gel2 scaffold were enhanced. A potent bactericidal solution of dendrimer-protected AgNPs was prepared at a concentration of 100 ppm. Three different amounts (100, 500 and 1000 μL) of this antibacterial solution were tested to identify the minimum inhibitory concentration necessary for effective bacterial control. Finally, a comprehensive evaluation of the scaffolds was performed through AgNPs release assays, disc diffusion antibacterial tests, cell toxicity assessments and cell attachment studies. The results indicated that the hAM/Gel2/S500 scaffold was the optimal specimen, demonstrating significant potential for controlling infections in wounds while promoting wound healing with minimal toxicity. This study highlights the promising application of the hAM/Gel2/S500 scaffold in regenerative medicine, particularly in wound management, and suggests directions for future research to further enhance its efficacy and applicability in clinical settings.

Data availability

All relevant experimental data supporting the findings of this study are included within the manuscript in the form of tables

and figures. Additional inquiries regarding the data may be directed to the corresponding author.

Conflicts of interest

There are no conflicts to declare.

Acknowledgements

The commercial hAM used in this study was prepared by the Iranian Tissue Products Co. (ITC), Iran. We extend our gratitude to Darman Andishan Marham (D&M) Co., Iran, for their support. Special thanks are also due to Dr Mazaher Gholipourmalekabadi for his insightful scientific comments regarding hAM. Finally, we would like to thank Ms. Anna-Katharina Schmid for her assistance in editing this manuscript.

Notes and references

1 M. C. O. Englund, P. Sartipy and J. Hyllner, *Regenerative Medicine*, Springer Netherlands, Dordrecht, 2011.
2 E. Taghiabadi, S. Nasri, S. Shafieyan, S. J. Firoozinezhad and N. Aghdami, *Cell J.*, 2015, **16**, 476–487.
3 A. Przekora, *Cells*, 2020, **9**, 1–29.
4 S. Dixit, D. R. Baganizi, R. Sahu, E. Dosunmu, A. Chaudhari, K. Vig, S. R. Pillai, S. R. Singh and V. A. Dennis, *J. Biol. Eng.*, 2017, **11**, 1–23.
5 Y. M. Bello, A. F. Falabella and W. H. Eaglstein, *Am. J. Clin. Dermatol.*, 2001, **2**, 305–313.
6 S. Davis, *Johns Hopkins Med. J.*, 1910, **15**, 307–396.
7 J. H. Arrizabalaga and M. U. Nollert, *ACS Biomater. Sci. Eng.*, 2018, **4**, 2226–2236.
8 M. Fénelon, S. Catros, C. Meyer, J. C. Fricain, L. Obert, F. Auber, A. Louvrier and F. Gindraux, *Membranes*, 2021, **11**, 1–27.
9 S. Iranpour, N. Mahdavi-Shahri, R. Miri, H. Hasanzadeh, H. R. Bidkhori, H. Naderi-Meshkin, E. Zahabi and M. M. Matin, *Cell Tissue Banking*, 2018, **19**, 357–371.
10 N. Fitriani, G. Wilar, A. C. Narsa, A. F. A. Mohammed and N. Wathoni, *Pharmaceutics*, 2023, **15**, 1–22.
11 G. Castellanos, Á. Bernabé-García, J. M. Moraleda and F. J. Nicolás, *Placenta*, 2017, **59**, 146–153.
12 R. Sarvari, P. Keyhanvar, S. Agbolaghi, L. Roshangar, E. Bahremani, N. Keyhanvar, M. Haghdoost, S. H. Keshel, A. Taghikhani, N. Firouzi, A. Valizadeh, E. Hamedi and M. Nouri, *J. Mater. Sci.:Mater. Med.*, 2022, **33**(3), 32.
13 M. Gholipourmalekabadi, M. Bandehpour, M. Mozafari, A. Hashemi, H. Ghanbarian, M. Sameni, M. Salimi, M. Gholami and A. Samadikuchaksaraei, *Burns*, 2015, **41**, 1488–1497.
14 K. Ramakrishnan and V. Jayaraman, *Burns*, 1997, **23**, S33–S36.
15 M. Parthasarathy, R. Sasikala, P. Gunasekaran and J. Raja, *J. Acad. Ind. Res.*, 2014, **2**, 545–547.
16 E. Inge, Y. P. Talmi, L. Sigler, Y. Finkelstein and Y. Zohar, *Placenta*, 1991, **12**, 285–288.
17 M. Gholipourmalekabadi, N. P. S. Chauhan, B. Farhadihosseinabad and A. Samadikuchaksaraei, in *Perinatal Tissue-Derived Stem Cells*, Springer, 2016, pp. 81–105.
18 N. G. Fairbairn, M. A. Randolph and R. W. Redmond, *J. Plast. Reconstr. Aesthetic Surg.*, 2014, **67**, 662–675.
19 A. Chopra and B. S. B. Thomas, *J. Biomimetics, Biomater., Tissue Eng.*, 2013, **18**, 1–8.
20 F. A. Tehrani, A. Ahmadiani and H. Niknejad, *Cryobiology*, 2013, **67**, 293–298.
21 R. Ramakrishnan, L. K. Krishnan, R. P. Nair and V. Kalliyana Krishnan, *Int. J. Polym. Mater. Polym. Biomater.*, 2020, **69**, 810–819.
22 L. Chen, X. Song, Z. Yao, C. Zhou, J. Yang, Q. Yang, J. Chen, J. Wu, Z. Sun, L. Gu, Y. Ma, S.-J. Lee, C. Zhang, H.-Q. Mao and L. Sun, *Biomaterials*, 2023, **300**, 122207.
23 S. P. Ndlovu, K. Ngece, S. Alven and B. A. Aderibigbe, *Polymers*, 2021, **13**, 2959.
24 B. S. Atiyeh, M. Costagliola, S. N. Hayek and S. A. Dibo, *Burns*, 2007, **33**(2), 139–148.
25 S. Liao, Y. Zhang, X. Pan, F. Zhu, C. Jiang, Q. Liu, Z. Cheng, G. Dai, G. Wu, L. Wang and L. Chen, *Int. J. Nanomed.*, 2019, **14**, 1469–1487.
26 H. Shi, H. Liu, S. Luan, D. Shi, S. Yan, C. Liu, R. K. Y. Li and J. Yin, *Compos. Sci. Technol.*, 2016, **127**, 28–35.
27 A. Haider and I.-K. Kang, *Adv. Mater. Sci. Eng.*, 2015, **2015**, 1–16.
28 M. Franckevičius, A. Gustainytė, R. Kondrotas, R. Juškėnas, M. Marcos, J. L. Serrano, R. Vaišnoras and V. Gulbinas, *J. Nanopart. Res.*, 2014, **16**, 2343.
29 L. Balogh, D. R. Swanson, D. A. Tomalia, G. L. Hagnauer and A. T. McManus, *Nano Lett.*, 2001, **1**, 18–21.
30 A. P. Dias, S. da Silva Santos, J. V. da Silva, R. Parise-Filho, E. Igne Ferreira, O. El Seoud and J. Giarolla, *Int. J. Pharm.*, 2020, **573**, 118814.
31 M. A. Mintzer and M. W. Grinstaff, *Chem. Soc. Rev.*, 2011, **40**, 173–190.
32 N. Wrońska, J. P. Majoral, D. Appelhans, M. Bryszewska and K. Lisowska, *Molecules*, 2019, **24**, 2894.
33 P. Rujitanaroj, N. Pimpha and P. Supaphol, *Polymer*, 2008, **49**, 4723–4732.
34 S. Khaliliazar, S. Akbari and M. H. Kish, *Appl. Surf. Sci.*, 2016, **363**, 593–603.
35 H. Klasen, *Burns*, 2000, **26**, 131–138.
36 A. G. Destaye, C.-K. Lin and C.-K. Lee, *ACS Appl. Mater. Interfaces*, 2013, **5**, 4745–4752.
37 M. A. Jebelli, E. Kalantar, A. Maleki, H. Izanloo, F. Gharibi, H. Daraei, B. Hayati, E. Ghasemi and A. Azari, *Jundishapur J. Nat. Pharm. Prod.*, 2015, **10**(3), e20621.
38 A. Castonguay and A. K. Kakkar, *Adv. Colloid Interface Sci.*, 2010, **160**, 76–87.
39 R. W. J. Scott, O. M. Wilson and R. M. Crooks, *J. Phys. Chem. B*, 2005, **109**, 692–704.
40 X. Sun, S. Dong and E. Wang, *Macromolecules*, 2004, **37**, 7105–7108.
41 G. Scott, *Degradable Polymers*, Springer, Dordrecht, Dordrecht, 2002.

42 Q. Tan, S. Li, J. Ren and C. Chen, *Int. J. Mol. Sci.*, 2011, **12**, 890–904.
43 Y. Pooshidani, N. Zoghi, M. Rajabi, M. Haghbin Nazarpak and Z. Hassannejad, *J. Mater. Sci.:Mater. Med.*, 2021, **32**(4), 46.
44 M. Pezeshki Modaress, H. Mirzadeh and M. Zandi, *Iran. Polym. J.*, 2012, **21**, 191–200.
45 F. Öfkeli, D. Demir and N. Bölgen, *J. Appl. Polym. Sci.*, 2021, **138**, 50337.
46 P. T. Sudheesh Kumar, V.-K. Lakshmanan, T. V. Anilkumar, C. Ramya, P. Reshmi, A. G. Unnikrishnan, S. V. Nair and R. Jayakumar, *ACS Appl. Mater. Interfaces*, 2012, **4**, 2618–2629.
47 P. Threepopnatkul, K. Vichitchote, S. Saewong, T. Tangsupa-Anan, C. Kulsetthanchalee and S. Suttiruengwong, *J. Met., Mater. Miner.*, 2010, **20**(3), 185–187.
48 S. Patel, U. Jammalamadaka, L. Sun, K. Tappa and D. Mills, *Bioengineering*, 2015, **3**, 1.
49 S. Bahrami, A. Solouk, H. Mirzadeh and A. M. Seifalian, *Composites, Part B*, 2019, **168**, 421–431.
50 M. Alim-Al-Razy, G. M. A. Bayazid, R. U. Rahman, R. Bosu and S. S. Shamma, *J. Phys.:Conf. Ser.*, 2020, **1706**(1), 12–20.
51 A. Amirjani, N. N. Koochak and D. F. Haghshenas, *J. Chem. Educ.*, 2019, **96**, 2584–2589.
52 B. Rao and R. C. Tang, *Adv. Nat. Sci.:Nanosci. Nanotechnol.*, 2017, **8**, 015014.
53 A. Amirjani, F. Firouzi and D. F. Haghshenas, *Plasmonics*, 2020, **15**, 1077–1082.
54 S. H. Salehi, K. As'adi, S. J. Mousavi and S. Shoar, *Indian J. Surg.*, 2013, 1–5.
55 V. Vivcharenko, M. Wojcik, K. Palka and A. Przekora, *Materials*, 2021, **14**, 1–21.
56 M. Kéri, A. Forgács, V. Papp, I. Bányai, P. Veres, A. Len, Z. Dudás, I. Fábián and J. Kalmár, *Acta Biomater.*, 2020, **105**, 131–145.
57 J. Xiao, Y. Ma, W. Wang, K. Zhang, X. Tian, K. Zhao, S. Duan, S. Li and Y. Guo, *Food Chem.*, 2021, **345**, 128802.
58 E. Chiellini, P. Cinelli, E. G. Fernandes, E.-R. S. Kenawy and A. Lazzeri, *Biomacromolecules*, 2001, **2**, 806–811.
59 R. Lanza, R. Langer and J. P. Vacanti, *Principles of Tissue Engineering*, Elsevier, 4th edn, 2014.
60 A. Mirtaghavi, A. Baldwin, N. Tanideh, M. Zarei, R. Muthuraj, Y. Cao, G. Zhao, J. Geng, H. Jin and J. Luo, *Int. J. Biol. Macromol.*, 2020, **164**, 1949–1959.
61 S. Chen, Q. Zhang, T. Nakamoto, N. Kawazoe and G. Chen, *Tissue Eng., Part C*, 2016, **22**, 189–198.
62 M. Sun, Y. Wang, L. Yao, Y. Li, Y. Weng and D. Qiu, *Polymers*, 2022, **14**(7), 1400.
63 D. A. Long, *J. Raman Spectrosc.*, 2004, **35**, 905.
64 S. Cavalu, G. Roiu, O. Pop, D. A. P. Heredea, T. O. Costea and C. F. Costea, *Materials*, 2021, **14**, 1–19.
65 R. Sripriya and R. Kumar, *Prog. Biomater.*, 2016, **5**, 161–172.
66 P. Gopinath, S. K. Gogoi, A. Chattopadhyay and S. S. Ghosh, *Nanotechnology*, 2008, **19**, 075104.
67 A. Ekhlasi, A. Solouk, M. Haghbin and P. Pasbakhsh, *Appl. Clay Sci.*, 2023, **243**, 107083.
68 M. Mahmoudi-Rad, E. Abolhasani, H. Moravvej, N. Mahmoudi-Rad and Y. Mirdamadi, *Clin. Exp. Dermatol.*, 2013, **38**, 646–651.
69 D. Shakiba, F. Alisafaei, A. Savadipour, R. A. Rowe, Z. Liu, K. M. Pryse, V. B. Shenoy, E. L. Elson and G. M. Genin, *ACS Nano*, 2020, **14**, 7868–7879.